

A selectivity filter mutation provides insights into gating regulation of a K⁺ channel

Theres Friesacher ^{1,5}, Haritha P. Reddy ^{2,3,5}, Harald Bernsteiner¹, J. Carlo Combista², Boris Shalomov², Amal K. Bera³, Eva-Maria Zangerl-Plessl¹, Nathan Dascal ^{2,4}✉ & Anna Stary-Weinzinger ¹✉

G-protein coupled inwardly rectifying potassium (GIRK) channels are key players in inhibitory neurotransmission in heart and brain. We conducted molecular dynamics simulations to investigate the effect of a selectivity filter (SF) mutation, G154S, on GIRK2 structure and function. We observe mutation-induced loss of selectivity, changes in ion occupancy and altered filter geometry. Unexpectedly, we reveal aberrant SF dynamics in the mutant to be correlated with motions in the binding site of the channel activator Gβγ. This coupling is corroborated by electrophysiological experiments, revealing that GIRK2_{wt} activation by Gβγ reduces the affinity of Ba²⁺ block. We further present a functional characterization of the human GIRK2_{G154S} mutant validating our computational findings. This study identifies an allosteric connection between the SF and a crucial activator binding site. This allosteric gating mechanism may also apply to other potassium channels that are modulated by accessory proteins.

¹Department of Pharmaceutical Sciences, Division of Pharmacology and Toxicology, University of Vienna, Josef-Holaubek-Platz 2, 1090 Vienna, Austria.

²Department of Physiology and Pharmacology, School of Medicine, Tel Aviv University, Tel Aviv 69978, Israel. ³Department of Biotechnology, Bhupat and Jyoti Mehta School of Biosciences, Indian Institute of Technology Madras, Chennai 600036, India. ⁴Sagol School of Neuroscience, Tel Aviv University, Tel Aviv 69978, Israel. ⁵These authors contributed equally: Theres Friesacher, Haritha P. Reddy. ✉email: dascaln@tauex.tau.ac.il; anna.stary@univie.ac.at

Potassium inward rectifier (K_{ir}) channels are key players in the regulation of the resting membrane potential. They constitute highly selective permeation pathways for K^+ ions across the cell membrane, which conduct inward currents more efficiently than outward currents. This phenomenon originates in a voltage-dependent block by intracellular Mg^{2+} and polyamines preventing excessive K^+ efflux¹. K_{ir} channels form homo- as well as heterotetramers, which are generally activated by phosphatidylinositol 4,5-bisphosphate (PIP_2)². Members of the K_{ir} 3 (GIRK) channel subfamily are additionally regulated by intracellular sodium and the $\beta\gamma$ subunits of the G-proteins, $G\beta\gamma$ (an obligatory dimer of $G\beta$ and $G\gamma$)³. The mechanism underlying the gating regulation of GIRKs by Na^+ , PIP_2 , and $G\beta\gamma$ is of great interest, since GIRKs have been shown to play crucial roles in a number of neurological processes, such as drug addiction, learning, and memory, as well as several neurological conditions, including Parkinson's disease, Down's syndrome, and epilepsy, turning them into crucial targets for drug development of neurological disorders⁴.

In general, K^+ permeation through the GIRK channel pore is restricted by three distinct regions: the selectivity filter (SF) containing the highly conserved amino-acid motive TIGYG, the helix bundle crossing (HBC) gate, and the G-loop gate at the apex of the cytoplasmic domain (Fig. 1). So far, diverse aspects of GIRK channel control have been unraveled^{5–12}, but consensus on a gating model has not been reached yet. For example, X-ray crystallography experiments^{5,6} suggest that HBC and G-loop gate opening is facilitated by PIP_2 and $G\beta\gamma$ in a co-dependent manner through a rotation of the C-terminal domain (CTD) and splaying of the inner helices. Interestingly, a crystal structure of GIRK2 bound to all of its activators does not capture a fully open channel, motivating the authors to propose a dynamic activated state, which fluctuates between non-conductive and conductive conformations⁶. Several MD simulation studies observe an influence of PIP_2 binding on the HBC gate^{7,8}. Li et al.⁹ hold $G\beta\gamma$ and Na^+ accountable for the opening of the G-loop gate and HBC gate, respectively, while reporting a stabilizing effect of PIP_2 binding on the open conformation of the gates. Another putative aspect of GIRK channel gating was revealed by Cryo-EM structures^{10,11}, which indicate that the CTD of the channel can adopt two different conformations: a docked and an extended

conformation that differ in the compactness as well as distance of the domain to the transmembrane part of the protein. PIP_2 binding leads to a switch from the extended to the docked conformation, making the channel susceptible towards $G\beta\gamma$ binding¹⁰. Such PIP_2 -dependent conformational changes have also been reported for other K_{ir} channels¹².

This study takes an approach towards investigating GIRK2 regulation by using a disease-causing mutation in the SF as a tool to look into allosteric connections governing channel activity. The mutation G154S in human GIRK2 (hGIRK2) is associated with a rare and severe neurological disorder, called the Keppen–Lubinsky syndrome (KPLBS, OMIM: 614098)¹³. While the biophysical properties of the disease mutant have not been studied yet, the corresponding mutation in mouse GIRK2 (mGIRK2) channels, the so-called *weaver* mouse model (mGIRK2_{ww})^{14–19}, is known for more than 30 years. Studies detected remarkable changes in mGIRK2_{ww} behavior, which is characterized by a loss of K^+ selectivity, insensitivity to blockage by extracellular Ba^{2+} and elevated basal activity^{14,16,17,19}. These severe abnormalities are linked to the death of cerebellar granule cells that underlies the disease symptoms of the *weaver* mouse^{15,20}.

Curiously, mGIRK2_{ww} has previously been reported to display impaired activation by $G\beta\gamma$ ^{14,17,19}. This raises the question about the role of the SF region in controlling GIRK2 activation by physiological stimuli. Despite its pathological importance, experimental characterization of the biophysical, physiological, and pharmacological properties of hGIRK2_{G154S} is still lacking.

In this work, we use μ s-long MD simulations to investigate the effect of the *weaver* mutation on mGIRK2, which we corroborate by a functional characterization of the corresponding human mutant, hGIRK2_{G154S}, with electrophysiology experiments. We provide insight into the functional, dynamic, and allosteric consequences of the SF mutation. We reveal that the mutation causes abnormalities in channel behavior and unveil SF alterations that provide mechanistic understanding of the loss of K^+ selectivity. By subsequently applying a functional mode analysis (FMA), we identify collective motions, which are coupled to aberrant SF dynamics in the mutant channel. The analysis uncovered an unexpected correlation between SF movements and dynamics in the $G\beta\gamma$ -binding site. This finding was corroborated by electrophysiological experiments that reveal an effect of $G\beta\gamma$ on hGIRK2_{wt} block by the pore blocker Ba^{2+} . Our study uncovers a novel aspect of GIRK2 gating, which is characterized by a coupling of the SF to a major regulator binding site.

Results

The *weaver* mutation leads to a loss of selectivity and efficiency of K^+ permeation. We conducted μ s-long MD simulations of the wild-type (mGIRK2_{wt}) and mutant (mGIRK2_{ww}) channel in order to investigate the consequences of the *weaver* mutation on channel dynamics. From here on, the mouse *weaver* mutant mGIRK2_{G156S} is termed mGIRK2_{ww} in order to avoid confusion with the hGIRK2 mutant G154S, here named hGIRK2_{G154S}. An open and conductive state from our previous simulations of the PIP_2 -bound mGIRK2_{wt} channel was extracted⁷ (PDB: 3SYA). The channels were simulated in mixed Na^+/K^+ salt conditions (90 mM KCl:90 mM NaCl) applying electric fields in the range of 40–60 mV nm⁻¹ in the outward direction. Supplementary Table 1 summarizes all runs and the observed ion permeation events. A total of 6 μ s simulation data with mGIRK2_{wt} unraveled a high selectivity for K^+ , yielding a permeability ratio p_{Na}/p_K of 0.025 ($p_K/p_{Na} = 40$). In contrast, 9 μ s simulation data of the mGIRK2_{ww} channel revealed an increase of p_{Na}/p_K to 0.31 ($p_K/p_{Na} = 3.22$) (Supplementary Table 1). Our results concur with a previous electrophysiological study that reports a P_K/P_{Na} ratio

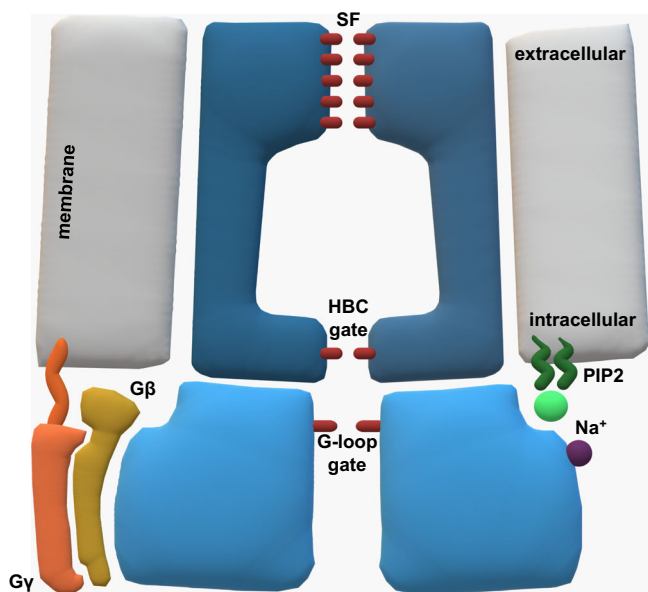


Fig. 1 The structure of the GIRK2 channel and its regulators. Two of the four subunits of the channel as well as channel modulators are illustrated.

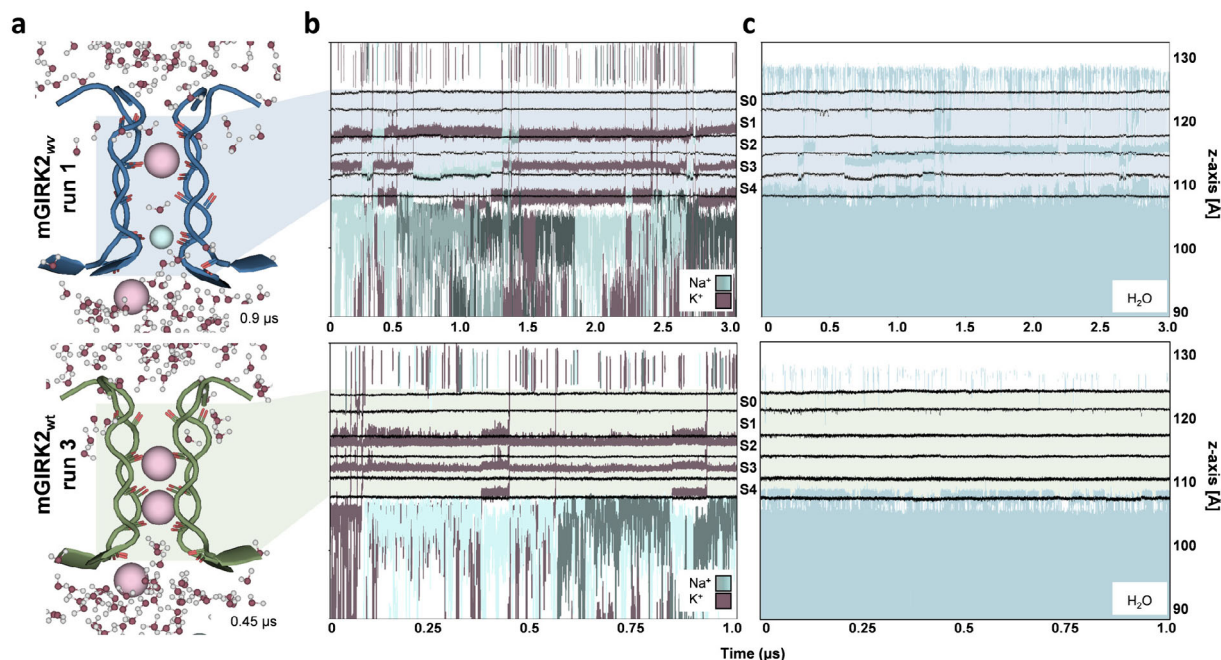


Fig. 2 Ion and water flux through the mGIRK2_{wv} (top) and mGIRK2_{wt} (bottom) SF over simulation time. **a** Representative snapshots of ion and water flux through the SF. mGIRK2_{wv} is colored blue, while mGIRK2_{wt} is colored green. The SF is depicted in cartoon representation with the backbone oxygens of the SF residues indicated as red sticks. K⁺ ions are represented as pink spheres, while Na⁺ ions are represented as smaller, light blue spheres. Water molecules are shown in a ball-and-stick representation. **b** K⁺ (purple) and Na⁺ ions (blue) flux observed in runs with mGIRK2_{wv} and mGIRK2_{wt}. Each line displays the position of one ion on the z-axis over simulation time. The positions of the backbone oxygens of the SF residues, which frame the canonical ion binding sites S0–S4, are shown in black. **c** Presence of water in the mGIRK2_{wv} and mGIRK2_{wt}. Each line displays the position of one water molecule on the z-axis over simulation time. The positions of the backbone oxygens of the SF residues are shown in black.

of ≥ 20 for the mGIRK2_{wt}, which is contrasted by P_K/P_{Na} ratios of ~ 2 for mGIRK2_{wv}¹⁹.

Figure 2b shows the outward permeation of ions and the presence of water in the mGIRK2_{wv} SF and mGIRK2_{wt} SF over simulation time. The most striking divergence between the simulations is the mutation-induced loss of selectivity for K⁺, which is demonstrated by several Na⁺ passing through the mGIRK2_{wv} SF. The relative Na⁺ permeation rate increases from 0.16 ions/ μ s for mGIRK2_{wt} to 2.25 ions/ μ s for mGIRK2_{wv}. Furthermore, our simulations unveil reduced K⁺ movement through the mutant channels, which is reflected in the drop of relative K⁺ permeation rates from 6.67 ions/ μ s for mGIRK2_{wt} to 1.4 ions/ μ s for mGIRK2_{wv}.

Interestingly, mGIRK2 conductance varies greatly between the different runs. In case of mGIRK2_{wv}, one of the six runs is accountable for 10 of 13 conduction events, while in four runs no ions permeated. Similarly, run 3 of the mGIRK2_{wt} shows extreme conductance. Hence, mGIRK2 is not steadily permeable in our simulations, but transiently adopts a conductive state allowing multiple ions to pass within a short period of time (Fig. 2 and Supplementary Fig. 1).

mGIRK2_{wt} block by Na⁺ was observed in three of the six wild-type runs. In mGIRK2_{wt} run 1 and run 6, ion flux is halted shortly after simulation start due to the binding of a Na⁺ ion between the sites S3 and S4 (Supplementary Fig. 1). In run 5, Na⁺ advances to site S2 and remains there stably bound, thereby inhibiting further ion permeation. The block of K⁺ flux by Na⁺ ions is in agreement with previous electrophysiology experiments and simulations studies^{19,21–23}.

In the simulations with mGIRK2_{wv}, it can be observed that raised Na⁺ permeation levels are accompanied by a deficient

exclusion of water from the SF. The right permeation plot in Fig. 2b shows water entering the mutant SF after about 250 ns simulation time, occurring simultaneously to the first Na⁺ permeation event. However, solvation is not tightly coupled to Na⁺ permeation, since water is also present in case only K⁺ occupies the SF (e.g., Fig. 2b between 1.5 and 2 μ s). On the contrary and in line with previous studies^{7,21,24}, no water can be seen in the simulations with mGIRK2_{wt}. K⁺ ions shed the water shell upon entering the SF and permeate in a dehydrated manner.

Experimental characterization of the hGIRK2_{G154S} reveals drastic changes in channel selectivity and regulation.

We used two-electrode voltage-clamp experiments to carry out the functional characterization of hGIRK2_{G154S} with the aim to investigate the effects of the SF mutation on human GIRK2 behavior. hGIRK2_{wt} and hGIRK2_{G154S} channels were expressed in *Xenopus* oocytes by injecting the corresponding RNAs. hGIRK2 activation was achieved by coexpression of G β γ ^{25,26}. We compared current amplitudes and current–voltage (I – V) relationships in 5 groups of oocytes either by expressing hGIRK2_{wt} with or without G β γ , or hGIRK2_{G154S} with or without G β γ , or naive oocytes (uninjected with any RNA).

Figure 3a shows a representative recording from oocytes expressing hGIRK2_{wt} with G β γ . The oocyte was sequentially exposed to four extracellular solutions containing 2, 8, 24, or 72 mM K⁺ and, correspondingly, 96, 90, 74, or 26 mM Na⁺. A voltage ramp from -120 to 50 mV was applied in each solution (Fig. 3b), yielding I – V curves (Fig. 3c). The same procedure was repeated in the four solutions containing 1 mM Ba²⁺, which is a pore blocker of K_{ir} channels^{23,27–29}. To allow comparison of

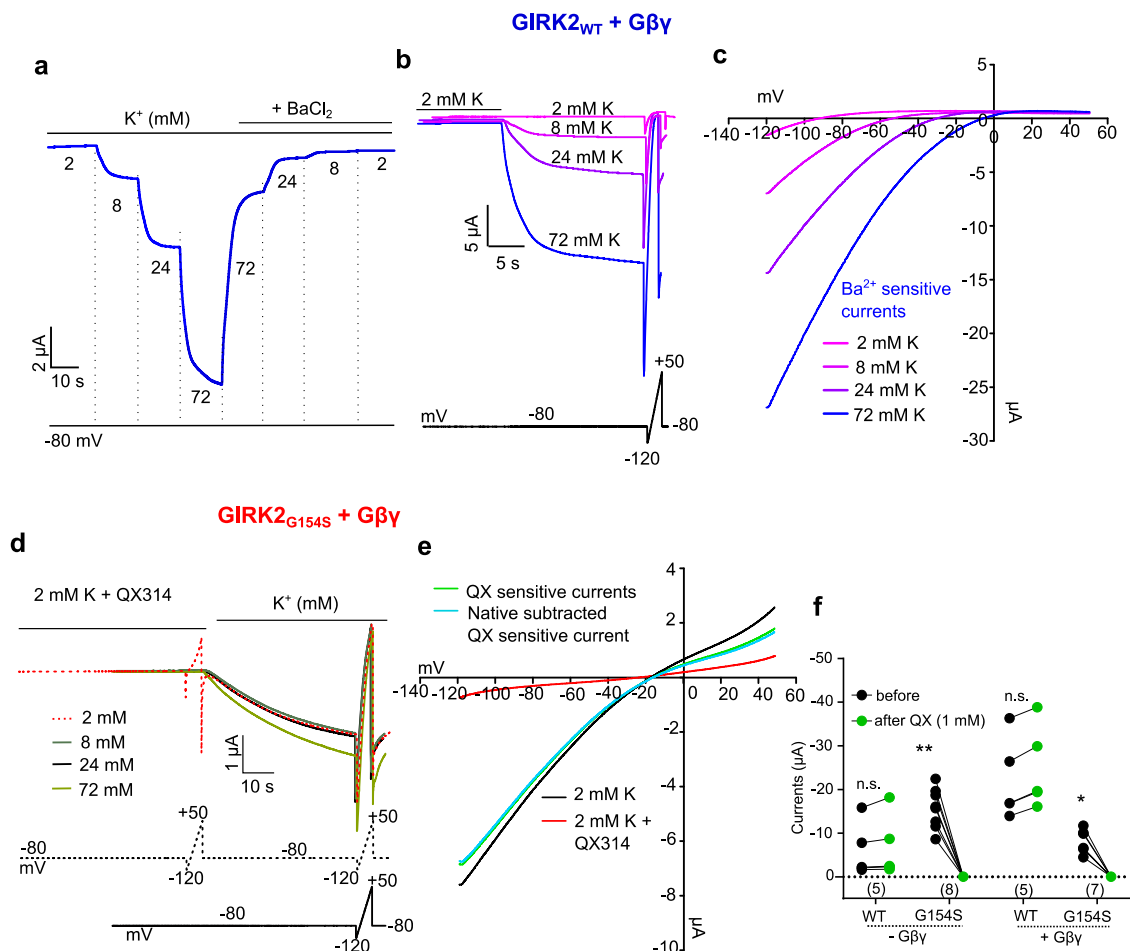


Fig. 3 hGIRK2_{G154S} compared to hGIRK2_{wt}. **a** Representative of whole cell current records from hGIRK2_{wt} with Gβγ. Sequential changes of solutions and subsequent Ba²⁺ block are shown. The holding potential was -80 mV, and the recording always started in low-K⁺ (2 mM) solution. **b** Representative recordings of whole-cell currents from hGIRK2_{wt} with Gβγ. 2 s voltage ramps from -120 to $+50$ mV are performed in each solution. Record from each solution is shown in a different color. Voltage protocol is shown in the lower panel. **c** I - V curves in a representative oocyte expressing hGIRK2_{wt} with Gβγ tested in four solutions. Ba²⁺ sensitive currents are shown. **d** Representative recordings of whole-cell currents from hGIRK2_{G154S} with Gβγ. 2 s voltage ramps from -120 mV to $+50$ mV are performed in each solution. **e** I - V curves in a representative oocyte expressing hGIRK2_{G154S} with Gβγ in the 2 mM K⁺ solution (black) along with QX block (red), QX sensitive currents (green) and the net QX currents obtained from subtracting average native currents from QX sensitive currents (cyan) are shown. **f** hGIRK2_{wt} and hGIRK2_{G154S} currents with and without Gβγ, before and after QX314 (1 mM) application, in 4–7 oocytes from one frog, are shown. Paired t -test followed by Wilcoxon test was performed. ** $p = 0.0078$ and * $p = 0.0156$; n.s. is not significant ($p > 0.05$).

current amplitudes between the different experimental groups and with previous publications^{30,31}, we used the values of inward currents at -80 mV in 24 mM K⁺ solution (Fig. 4a).

In line with previous studies³⁰, uninjected oocytes showed small, mostly leak currents of -51 ± 4 nA ($n = 5$, Supplementary Fig. 2a), and only a minor fraction (2 ± 1 nA, $n = 5$) was blocked by Ba²⁺. In contrast, currents in hGIRK2_{wt} and hGIRK2_{wt} + Gβγ groups were almost fully blocked by Ba²⁺, therefore net hGIRK2_{wt} I - V curves were obtained by subtracting Ba²⁺-insensitive currents²⁶ (Fig. 3c and Supplementary Fig. 2b–d). As expected, hGIRK2_{wt} showed inward currents and strong inward rectification both in the presence (Fig. 3c) and absence (Supplementary Fig. 2c) of Gβγ, which were increased in amplitude with increased [K_o] (Figs. 3b and 4b). In contrast, hGIRK2_{G154S} yielded large basal currents (Figs. 3d, e, 4a, b and Supplementary Fig. 2e–g), similar to its mouse counterpart, the mGIRK2_{wv}¹⁶. The amplitude of hGIRK2_{G154S} currents, both with or without Gβγ, was >80 times greater than in native oocytes (-4.2 ± 0.4 μA ($n = 6$) and -6.5 ± 1.5 μA ($n = 6$), respectively) (Fig. 4a). Therefore, for further analysis, we assumed that the total current measured in these cells represents the net hGIRK2_{G154S}

current with $>95\%$ accuracy. I - V curves of hGIRK2_{G154S} with or without Gβγ showed little rectification (Fig. 4f) and reduced block by Ba²⁺ ($\sim 60\%$ block at 1 mM Ba²⁺, compared to full block of hGIRK2_{wt}) (Supplementary Fig. 2g). Similar behavior was previously reported for the mouse *weaver* mutant, which was also observed to be blocked by the cation channel blocker QX314^{14,19}. Accordingly, GIRK2_{G154S} was blocked by $99.6 \pm 0.1\%$ by 1 mM QX314, while hGIRK2_{wt} was unaffected by QX314 (Fig. 3f).

Figure 4 shows the quantitative analysis of whole-cell hGIRK2_{wt} and hGIRK2_{G154S} currents. As previously reported for mGIRK2_{wt}³⁰, hGIRK2_{wt} yielded small I_{basal} , -194 ± 49 nA ($n = 5$) and showed strong, >18 fold activation by coexpressed Gβγ (-3.6 ± 1.7 μA, $n = 6$). In contrast, hGIRK2_{G154S} yielded a very large I_{basal} , which was not significantly increased by the coexpression of Gβγ (Fig. 4a). As noted above, hGIRK2_{wt} currents rised in amplitude with increased [K_o] (K⁺ was replacing Na⁺ in the external solution), whereas hGIRK2_{G154S} currents were almost insensitive to [K_o] (Fig. 4b), suggesting that K⁺ was not the sole carrier of the inward current at -80 mV. Figure 4c shows the dependence of the reversal potential (V_{rev}) of

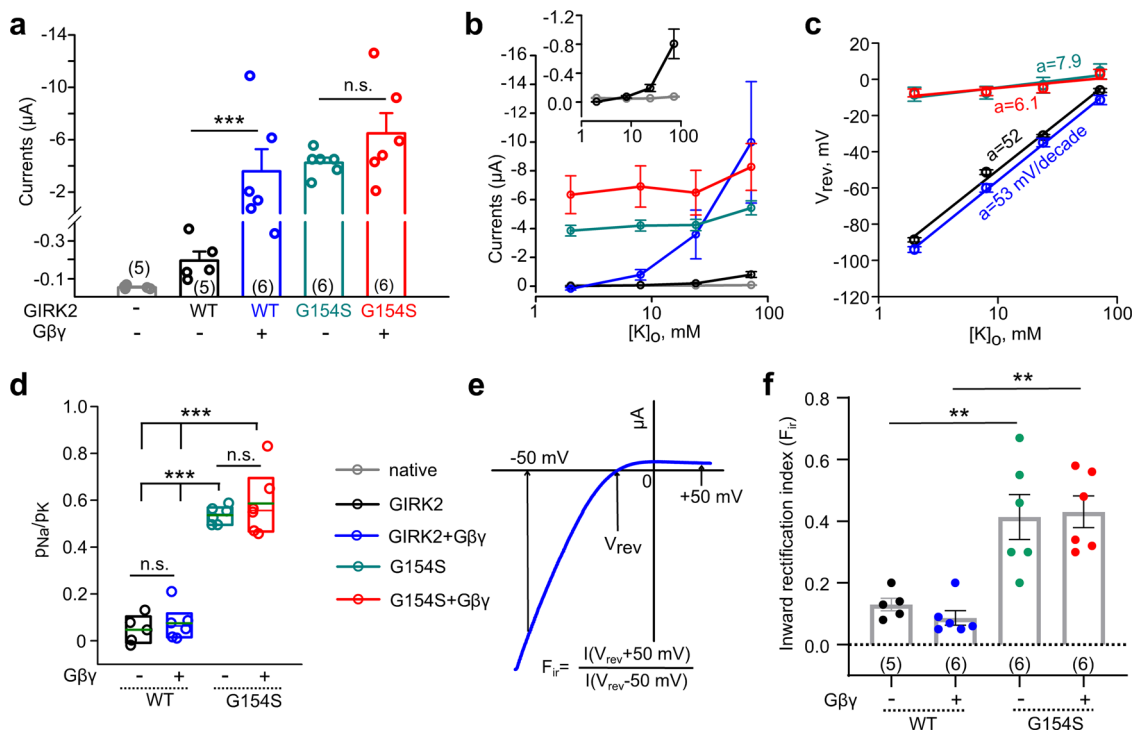


Fig. 4 hGIRK2_{G154S} channels are constitutively active and lose selectivity to K⁺. **a** Comparison of current amplitudes at -80 mV in 24 K⁺. G $\beta\gamma$ activates hGIRK2_{wt} (unpaired two-tailed *t*-test) but not hGIRK2_{G154S}. $n = 5$ – 7 oocytes (from one frog) in each group. The data in the bar graphs, here and in **f**, are presented as mean \pm SEM. **b** Changes in current amplitudes as a function of external K⁺ (note that K⁺ isotopically replaced Na⁺, Cl⁻ was kept constant). The inset zooms on native and hGIRK2_{wt} groups that showed lower currents. **c** The dependence of V_{rev} on [K_o]. Note the log scale of the X-axis. The slopes (**a**; mV/decade) of the linear least square regression lines are indicated near each line. Data are shown as mean \pm SEM from 6 to 7 oocytes in each group, from one frog. **d** p_{Na}/p_K permeability ratios, calculated from the reversal potentials obtained in 8 and 72 mM K⁺ solutions, in the four test groups. Kruskal-Wallis one-way ANOVA on ranks, followed by Dunn's pairwise multiple comparison test. In box plots, boxes show 25th and 75th percentiles. The horizontal lines colored as the box show the median, the green line shows the mean. *** $p < 0.001$. **e** An example of calculation of the rectification index, F_{ir} . **f** Comparison of F_{ir} of hGIRK2_{wt} and hGIRK2_{G154S} channels with and without G $\beta\gamma$. ** $p = 0.0065$ and 0.0022 . Numbers of oocytes tested are indicated below the bars.

hGIRK2_{wt} and hGIRK2_{G154S} on [K_o] (note the log scale on the X-axis). For hGIRK2_{wt}, V_{rev} was linearly related to $\log[K_{o}]$, with a slope of the $V_{rev}-\log[K_{o}]$ curve of 52–53 mV per 10-fold change in [K_o] (decade), close to the predicted slope of 58 mV/decade for a perfect K⁺ channel. Inversely, for hGIRK2_{G154S}, the change in V_{rev} was rather small, with a slope of 6–8 mV/decade, supporting lack of selectivity for K⁺. We subsequently calculated the permeability ratios for K⁺ to Na⁺, $r = p_{Na}/p_K$, by comparing the values of V_{rev} in two solutions containing different concentrations of Na⁺ and K⁺. The calculated values of p_{Na}/p_K for the 8–72 mM K⁺ pair are shown in Fig. 4d. In presence of G $\beta\gamma$, p_{Na}/p_K ratios of 0.029 ± 0.004 ($n = 6$) for hGIRK2_{wt} and 0.59 ± 0.05 ($n = 7$) for the hGIRK2_{G154S} were calculated. In case G $\beta\gamma$ was not co-expressed, we assessed p_{Na}/p_K of 0.05 ± 0.01 ($n = 5$) and 0.52 ± 0.04 ($n = 6$) for hGIRK2_{wt} and hGIRK2_{G154S}, respectively. Importantly, these ratios are in good agreement with our G $\beta\gamma$ -free simulations, which yielded p_{Na}/p_K ratios of 0.025 and 0.31 for hGIRK2_{wt} and hGIRK2_{G154S}, respectively. Additionally, the 20–30 fold higher p_K relative to p_{Na} for hGIRK2_{wt} is in good agreement with a previous report¹⁹.

We also quantified the extent of inward rectification (F_{ir}) (Fig. 4e, f). F_{ir} of hGIRK2_{wt} channels in presence and absence of G $\beta\gamma$ was 0.08 ± 0.009 ($n = 6$) and 0.13 ± 0.009 ($n = 5$), respectively, indicating strong inward rectification. For hGIRK2_{G154S}, we calculated F_{ir} values of 0.41 ± 0.02 ($n = 6$) with G $\beta\gamma$ and 0.43 ± 0.02 ($n = 6$) without G $\beta\gamma$, indicating a loss of rectification.

Ion occupancies in the mutant SF are shifted towards the extracellular site. Since an important aim of this framework is to elucidate not only the functional consequences of the SF mutation, but also the mechanism behind the channel malfunction, we undertook further analysis of our MD simulations focusing on the impact of the mutation at an atomistic scale. In a first step, we compared the ion occupancies in the SF, which unveiled clear differences between the wild-type and the mutant channel (Fig. 5a). In the mGIRK2_{wt} SF, K⁺ mainly populates the binding sites S2 and S3. The latter is also occupied in mGIRK2_{wv}, while the peak at S2 is shifted towards the extracellular site, so that K⁺ binds at an in-plane binding-pose between the canonical ion binding sites S1 and S2, at the level of the mutated residue S156. Interestingly, the same site is extensively occupied by Na⁺ in mGIRK2_{wt}, which, together with another in-plane conformation between sites S3 and S4, originates in the blockage of mGIRK2 by Na⁺ ions. The occupation of positions between classical binding sites by non-K⁺ ions has also been described in previous studies^{21,32–35}. On the contrary, negligible Na⁺ occupancies in the mGIRK2_{wv} SF can be observed, which indicates lower energy barriers for Na⁺ permeation and are interpretable as the basis for enhanced Na⁺ permeation rates.

S156 can form hydrogen bonds with the backbone oxygen of I155 and water molecules behind the SF. A closer investigation of the SF revealed that the mutant channel gains the ability to form a hydrogen bond between the sidechain of the mutated

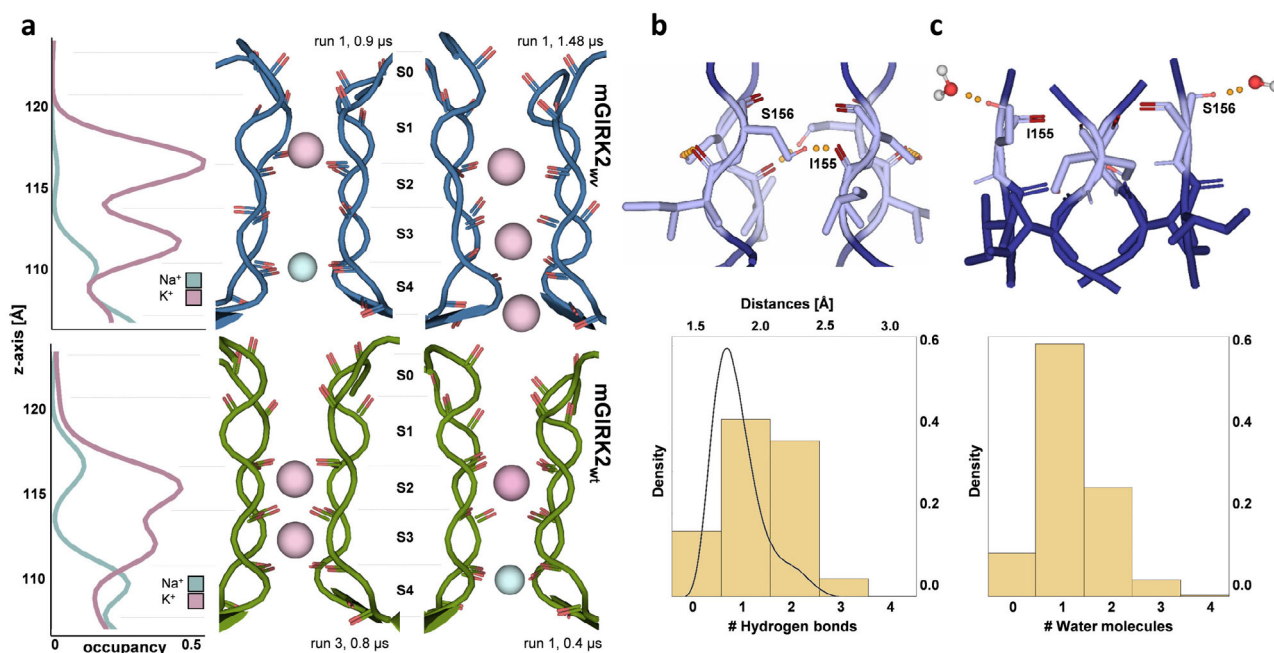


Fig. 5 Differences in ion occupancies and in the hydrogen bond network between mGIRK2_{wt} and mGIRK2_{wv}. **a** Top: Ion occupancies in the mGIRK2_{wv} SF observed over a total of 9 μ s-long MD simulation. Two characteristic snapshots of Na⁺ and K⁺ permeation are shown on the right. Bottom: Ion occupancies in the wild-type SF observed over 6 μ s long MD simulations. The snapshots on the right show a characteristic K⁺ occupancy pattern as well as Na⁺ block between sites S3 and S4. **b** Top: Representative snapshot of hydrogen bonds between the sidechain of S156 and the backbone oxygen of I155 in the mGIRK2_{wv} SF. Bottom: Density distribution of the distances and the numbers of hydrogen bonds between the sidechain of S156 and the backbone oxygen of I155 observed over 9 μ s simulations with GIRK2_{wv}. **c** Top: Representative snapshot of hydrogen bonds between the sidechain of S156 and a water behind the mGIRK2_{wv} SF. Bottom: Histogram of the number of water molecules behind the SF, which form hydrogen bonds to the sidechain of S156, over 9 μ s simulations with mGIRK2_{wv}.

residue S156 and the backbone oxygen of I155 (Fig. 5b). Looking at the occurrence of this interaction in the simulations with mGIRK2_{wv}, it can be seen that the hydrogen bond exists between one or two subunits for a substantial fraction of the simulation frames. The plot at the bottom of Fig. 5b shows a histogram of the number of hydrogen bonds as well as the distribution of the distances between S156 and the backbone oxygen of the I155. The latter displays an accumulation of the distances between 1.5 and 2 \AA , further confirming the importance of this interaction. Moreover, the sidechains of S156 were observed to form hydrogen bonds with water molecules, which occasionally diffuse behind the SF (Fig. 5c). Subsequent investigations revealed that this kind of interaction is most commonly established by one of the four subunits during the simulation. The mGIRK2_{wt} SF harbors a glycine at this site and hence lacks these functionalities.

The HBC gate is not affected by the SF mutation. In order to analyze whether the HBC gate is influenced by the SF mutation, we measured the distances between F192 of opposing subunits. For both mGIRK2_{wt} and mGIRK2_{wv}, the distribution of distances between opposing F192 Ca atoms culminates at about 18.5 \AA , while the peak of the minimum distance between opposing F192 residues is at around 11 \AA (Supplementary Fig. 23). In order to identify the motions in the channel maximally correlated with the movements of the HBC gate, Functional Mode Analyses (FMAs) were conducted. FMA models were constructed using the minimum distances between opposing F192 residues and the distances between F192 Ca atoms as functional quantities. None of the models obtained for mGIRK2_{wv} or mGIRK2_{wt} exceeded correlation measures of 0.23 in cross-validation. Thus, the MD

simulations show that the HBC gate is open to a similar degree in mutant and wild-type mGIRK2 and its movements are not correlated to any other motions in the ion channel. However, it should be emphasized that an open state of mGIRK2 was used as starting point of the simulations⁷. A coupling of the SF movement as well as an impact of the mutation on a more closed HBC gate can therefore not be excluded and remains to be elucidated in future studies.

Mutation-induced structural differences in the SF are associated with movements in the G β -binding site. In order to obtain detailed insight into the structural mechanisms underlying the alterations in ion selectivity and occupancies, we analyzed the geometry of the wild-type and mutant SF in detail. For this purpose, ϕ angles as well as inter-subunit distances of Ca atoms of the SF composing residues 154–158 were monitored over time (Fig. 6b). Analysis of the ϕ angle distribution revealed a striking difference at the mutated residue S156, displaying a pronounced peak at +60°, which is also sampled in mGIRK2_{wt} for G156, as well as a peak at -60°. It is likely that this new conformation is a side effect of the hydrogen bond between the S156 sidechain and the backbone oxygen of I155, which was identified as a quality of the mutant SF (Fig. 5b). Apart from the S156, reorientation of the carbonyl oxygen atoms away from the conduction pore is rarely observed. Some conformational flexibility can be seen at the extracellular entrance of the SF, as well. However, this plasticity at the threonine 154 occurs independently of the SF mutation in both mGIRK2_{wt} and mGIRK2_{wv}.

When looking at the distances between the Ca atoms of the SF-lining residues, it is noticeable that the mutant exhibits a wider

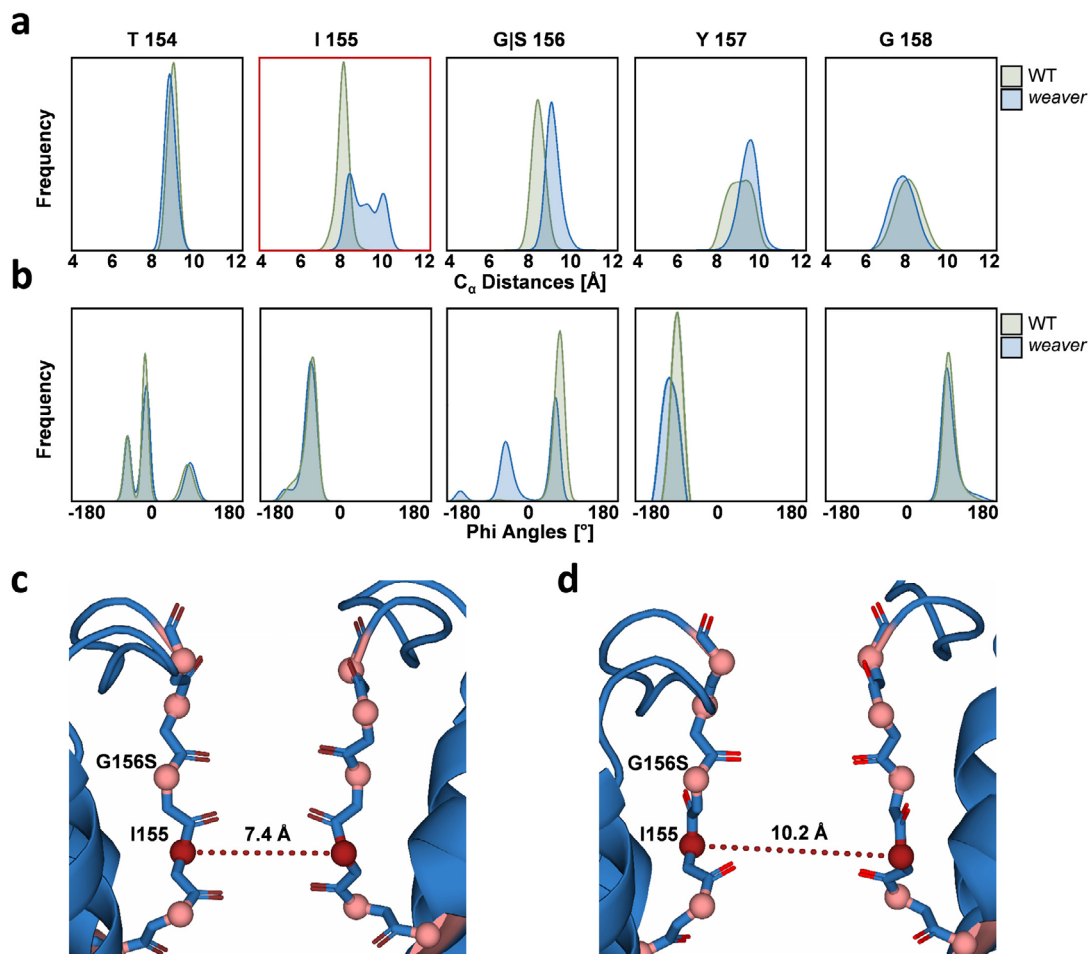


Fig. 6 Structural aberrations in the SF observed over 9 μ s mGIRK2_{wt} and 6 μ s mGIRK2_{wt} simulation. a Distributions of distances between C α of opposing mGIRK2 SF residues. **b** Phi-angle distributions of mGIRK2 SF residues. **c** and **d** mGIRK2_{wt} SF conformations showing the minimum (**c**) and maximum (**d**) distance between opposing I155 C α atoms. The C α atoms of I155 is highlighted are shown in dark red. Other C α atoms of the SF residues are shown as salmon spheres.

conformation at the residues 155–157, which confine the ion binding sites S2 and S3 within the SF filter (Fig. 6a). This difference is most pronounced for the isoleucine 155, which displays a bimodal distribution of inter-subunit distances with the two extremes about 2 Å apart (Fig. 6c). Considering the importance of SF geometry of K⁺ channels for selectivity and activity^{32,36}, this change in the SF conformation is drastic and is likely to provoke profound alterations in channel behavior. In our simulations, the dilation might play a profound role in the decrease in K⁺ selectivity and an enhanced accessibility of the SF for water molecules.

In order to elucidate the dynamic consequences of the aberrant motions in the mGIRK2_{wt} SF, we used the functional mode analysis (FMA) tool³⁷ to identify the collective motion maximally correlated with I155 fluctuation. For this purpose, movements of the protein backbone were analyzed. The highly dynamic extracellular loop (residues 120–133) and C-terminus (residue 369–382) were excluded in order to reduce the background noise. Remarkably, the FMA identified mainly movements in the C-terminal domain (CTD) of mGIRK2_{wt} to be linearly correlated with the I155 distance fluctuations (Fig. 7). Cross-validation of the model yielded a Pearson *R* of 0.73 (Fig. 7d).

When taking a closer look at the correlated movements in the CTD, it can be seen that the region determined to be most affected by I155 distance fluctuations comprises the residues

247–254. Importantly, these amino acids constitute the β D- β E loop of the GIRK2 CTD, which, together with the β L- β M loop of the adjacent subunit, composes the G β γ -binding site in the G β γ -mGIRK2 crystal structure⁶ (Fig. 7b). The SF and the G β γ -binding site are located at the upper region of the transmembrane domain and at the inferior side of the CTD, respectively, resulting in a distance of about 75 Å. In spite of the spatial segregation, the regions separating the SF and the G β γ -binding site seem to be largely unaffected by the dynamics of I155 indicating that the correlation is not the result of a mutation-induced global rearrangement, but an allosteric coupling between the mutant SF and a crucial regulatory site.

The FMA identified further correlated movements at the lowest part of the inner loops of the CTD around the residue Y267 (Fig. 7b). An involvement of this region in channel regulation is not supported by the literature. Nevertheless, a regulatory function cannot be entirely excluded due to its crucial location at the intracellular entry of the GIRK2 pore. Moreover, less pronounced coupling could be seen in the lower part of the transmembrane helix 1 and the region below the tether helix (Fig. 7c).

An FMA of I155 dynamics in mGIRK2_{wt} could not unveil significant correlations with any part of the channel (Fig. 7d, Pearson *R* ~ 0.35). A possible explanation for the absence of correlation might be that the coupling between the SF and the

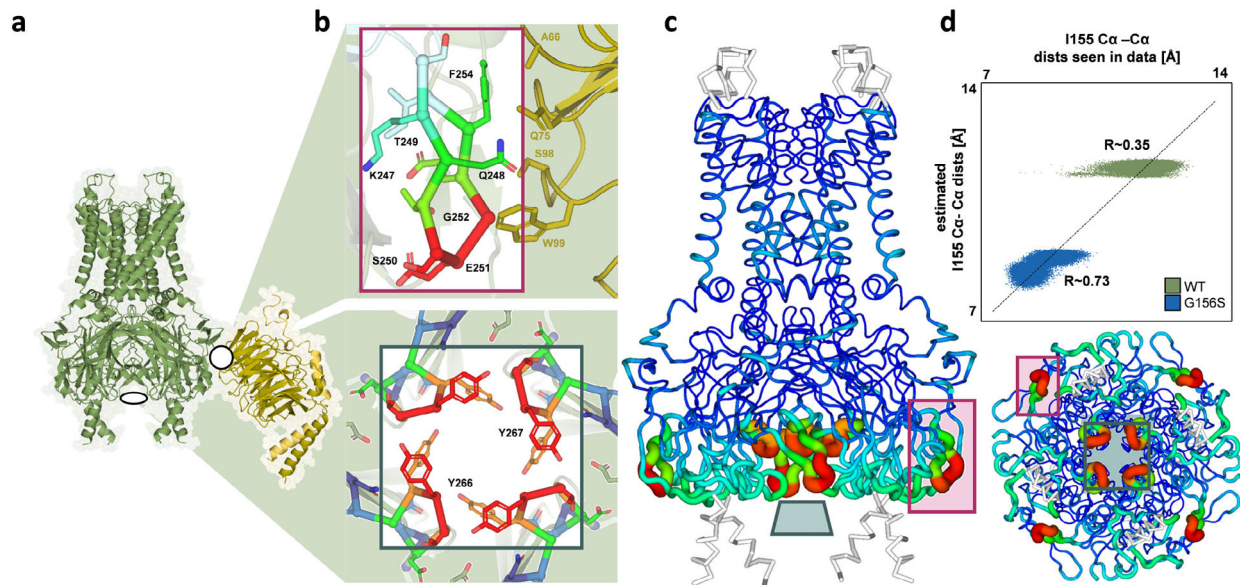


Fig. 7 Functional mode analysis (FMA) of the aberrant SF fluctuations at I155 of mGIRK2_{wv}. **a** Gβγ-bound mGIRK2_{wt} according to the 4KFM crystal structure. mGIRK2 is shown in green, one Gβγ subunit is shown in shades of orange. **b** Close-ups of the two regions, which were seen to be most affected in the FMA model. The top figure depicts a side view of the Gβγ-binding site. The lower figure shows a bottom-up view of the inner loops of the CTD. The colors of the residues correspond to the colors allocated in the FMA model in **(c)**. **c** Correlations predicted by the FMA model projected on the side (left) and on the bottom-up (bottom right) view of mGIRK2. The backbone of mGIRK2 is shown in rainbow colors. Red indicates a high correlation of movements in the respective region to the Cα distance fluctuation of I155, while blue indicates no correlation. White parts were not considered in FMA model calculation. The close-ups shown in **b** are indicated with purple and cyan rectangles for the Gβγ binding site and the inner loops of the CTD, respectively. **d** Validation plot of the FMA of MD simulations with the mGIRK2_{wt} and mGIRK2_{wv} channel.

CTD is a feature unique to mGIRK2_{wv}. However, it has to be mentioned that the mGIRK2_{wt} SF is much less dynamic than the mutant SF in our simulations. The distance fluctuations of I155 in the wild-type SF might be too small to be linked to any other movements, hence hampering the detection of coupled collective motions. For mGIRK2_{wt}, future simulations with Gβγ-bound GIRK2, which go beyond the scope of this study due to the inherent computational effort, might be necessary to make traces of a coupling between the SF and the Gβγ-binding site visible.

Ba²⁺ block as sensor to test Gβγ-induced changes in SF dynamics. Ba²⁺ is a high-affinity pore blocker of inwardly rectifying K⁺ channels, including GIRK^{23,27–29}, which blocks the pore by interacting with the SF^{29,38} mainly at site 4³⁹. Motivated by our computational findings, we deemed it possible that Ba²⁺ may serve as a sensor of Gβγ-induced changes in SF dynamics. To test this hypothesis, we measured the parameters of Ba²⁺ block of hGIRK2_{wt} in oocytes that expressed the channel alone, or hGIRK2_{wt} with Gβγ. Ba²⁺ blocked the basal hGIRK2_{wt} currents in a dose-dependent manner with an IC₅₀ of 26.4 ± 1.4 μM (Fig. 8). In the presence of Gβγ, the affinity of block was about 2.5 times lower, the IC₅₀ was 66.9 ± 8.2 μM. These findings are in line with our hypothesis of a coupling between the SF and the Gβγ-binding site, as suggested by our MD simulations.

Discussion

Gating of K⁺ channels occurs in response to channel-specific stimuli, which in the context of K_{ir} channels is facilitated by PIP₂,

as well as various additional regulators, such as Na⁺, Gβγ, ethanol, ATP, and sulfonylurea receptor subunits. Most of these ligands do not interact with the pore domain directly, but induce gating changes by binding to regulatory domains. In case of GIRK channels, Na⁺ and Gβγ bind to different regions at the CTD, which leads to physical changes at the gates and to a release of steric constrictions impeding K⁺ flux.

Previous studies^{5–10,40–42} have identified ligand-dependent conformational changes important for GIRK2 activity and suggest a complex allosteric network connecting the gates and the modulatory binding sites. Consensus exists about the relevance of large scale movements, such as rotation and rocking of the CTD and bending of transmembrane helix 2 for channel activity, while several aspects about the detailed coupling underlying channel opening have been revealed^{6–11}.

In an effort to gain a fresh perspective on GIRK2 regulation, we choose an alternative approach to shed light on the allosteric consequences of Gβγ binding by making use of the well-studied *weaver* mouse mutant (mGIRK2_{wv})^{14–20,43}, which carries a mutation in the SF. Importantly, this mutation does not only drastically alter channel selectivity, but produces an aberrant basal inward current that lacks G-protein activation^{14,16,19}.

Analysis of μs-long MD simulations suggest a coupling between the SF and the Gβγ-binding site in mGIRK2_{wv}. More specifically, functional mode analysis (FMA) unveiled a correlation of aberrant SF dynamics at residue I155 with movements of residues previously reported to contact Gβγ⁶ (Fig. 7). Thus, our computational results indicate that mutation-induced changes in the SF are translated to conformational changes in the

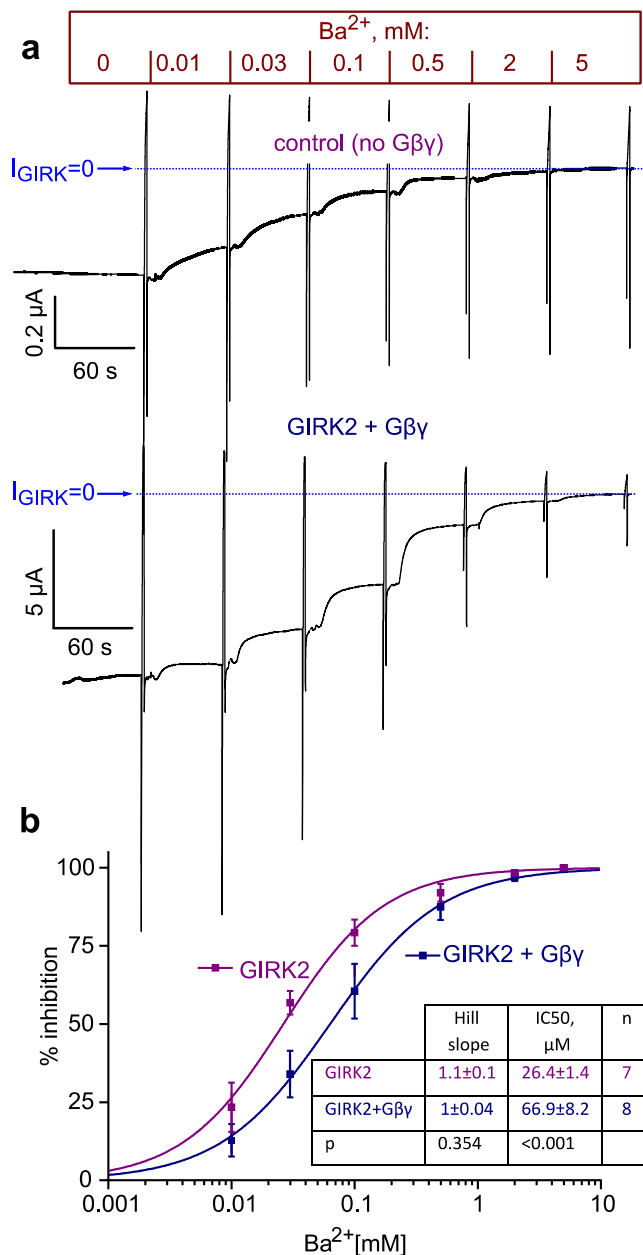


Fig. 8 Ba²⁺ block is altered following activation of hGIRK_{2wt} by Gβγ.

a Representative records of Ba²⁺ dose-response experiments in oocytes expressing hGIRK_{2wt} (upper trace) or hGIRK_{2wt} + Gβγ (lower trace). The currents were measured at -80 mV. A voltage ramp was applied toward the end of each episode with the indicated Ba²⁺ concentration, and after that the solution was switched to the next, higher Ba²⁺ concentration. **b** Summary of the experiment. Averaged normalized data (% of current inhibition) are shown as mean ± SEM. These averaged dose-response relationships were fitted to the Hill equation (Eq. (9), see the “Methods” section) with the following parameters: hGIRK₂, h (Hill slope) = 1.053, IC₅₀ = 26 μM; hGIRK₂ + Gβγ, h = 0.98, IC₅₀ = 63 μM. In addition, in each oocyte, the dose-response relationship was fitted separately to the Hill equation. Average parameters (h and IC₅₀) are shown in the table (inset). Statistical analysis was done using t -test (Hill slope) and Mann-Whitney test (IC₅₀).

Gβγ-binding site. To further test this correlation, we performed electrophysiological experiments with the human GIRK_{2G154S} channel, which carries a disease-causing mutation corresponding to the *weaver* mutation. We found that, as expected, hGIRK_{2G154S}

channels are constitutively active and cannot be further activated by Gβγ. Therefore, hGIRK_{2G154S} displays a behavior reminiscent of mGIRK_{2_{wv}} and is likely to experience a similar coupling between SF and the Gβγ regulatory site.

Ba²⁺ is a high-affinity blocker of K⁺ channels including GIRK_{23,27-29}, which blocks the pore by interacting with the SF^{29,38} mainly at site 4³⁹. Given the location of the binding site in the SF, we deemed it possible that Ba²⁺ serves as a sensor of Gβγ-induced changes in SF dynamics. Our electrophysiological experiments show that Gβγ activation of hGIRK_{2wt} is accompanied by a ~2.5-fold decrease in the affinity of Ba²⁺, compared to hGIRK_{2wt} alone. Importantly, this finding corroborates the presence of an allosteric link between the SF and the Gβγ-binding site in wild-type hGIRK₂ channels, as well.

The concept of allosteric networks connecting diverse gating regions, including the SF, and modulatory sites is well-established in the field of K⁺ channel regulation. For example, conformational changes in the SF, which affect channel conductivity, have been observed to allosterically influence an inner gate in MthK⁴⁴, KcsA⁴⁵ and NaK⁴⁶ channels. However, much less is known about the interplay between ligands binding to intracellular domains and gating at the SF. One such coupling was observed for the K2P channel TREK-2, which is allosterically activated at the SF by binding of the small molecule 2-Aminoethoxydiphenyl borate to the proximal C-terminus⁴⁷.

Recently, Chen et al.⁴⁸ suggested coupling between the SF and the Gβγ-binding site of mGIRK₂ based on electrophysiology experiments that revealed mGIRK_{2_{wv}} stimulation by the channel activator Ivermectin, but not the Gβγ-mediated pathway. Furthermore, Li et al.⁴² described the GIRK₂ SF as a crucial determinant for K⁺ permeation, which can be influenced by binding of Gβγ and Na⁺. In line with these studies, our findings demonstrate a coupling between the GIRK₂ SF and the Gβγ binding site corroborated by both experimental and computational data. Against this background, we put forward a new aspect of GIRK₂ gating by extending the role of the SF from a mere energy barrier to a Gβγ-controlled gating region, thereby adding it to the classical gates controlling K⁺ permeation.

MD simulations with mGIRK_{2_{wv}} show that the mutation G156S leads to aberrant movements and an altered geometry of the SF (Figs. 5b, c and 6), which are likely to affect inherent features of the ion channel, such as selectivity and conductivity. Moreover, the mutation might alter the coupling between the SF and Gβγ-binding site, thereby providing a possible explanation for the impaired mGIRK_{2_{wv}} activation by Gβγ observed in experiments^{14,17,19}. However, it is unclear whether the mutation changes the affinity of modulators binding to the Gβγ-binding site, such as ethanol or the Gβγ subunit. This aspect remains to be elucidated in future studies, since the required modeling is beyond the scope of this framework.

Given the fact that the SF has been observed to couple to channel gating regions in a number of different K⁺ channels⁴⁴⁻⁴⁶, we analyzed the effect of the SF mutation on the HBC gate by measuring the minimum distances between opposing F192 residues as well as F192 Ca atoms. In addition, previous studies on GIRK channels provided evidence for an allosteric control of the HBC gate by Gβγ binding at the CTD^{9,49}. Aiming to clarify the role of the HBC gate in the coupling between the SF and the Gβγ binding site, FMAs were carried out to identify movements in the channel correlated to the motions of the HBC gate. At this point it should be stressed that a conductive state of mGIRK_{2wt} was used as starting point of the simulations and conclusions drawn from these analyses are hence limited to the open HBC gate. Distances at the HBC gate region did not differ in simulations with mGIRK_{2wt} and mGIRK_{2_{wv}} (Supplementary Fig. 3), and we could not identify correlations between HBC gate motions and

other movements within the channel. Thus, our data does not provide evidence that the open HBC gate is affected by the SF mutation or involved in the coupling between the SF and the G β binding site. Further investigations are needed to clarify these aspects for other HBC gate conformations and dynamics.

MD simulations performed in this study do not take into account the role of the CTD conformation in GIRK2 gating, as it was recently suggested by Cryo-EM structures¹⁰. More precisely, the CTD was reported to switch from an extended to a docked conformation upon PIP₂ binding, which makes GIRK2 susceptible to G β binding. Since modeling of the different CTD conformations is beyond the scope of this study, it remains to be elucidated how the coupling between the SF and the G β -binding site is influenced by conformational changes of the CTD, or whether conformational changes of the CTD themselves affect the SF. However, the MD simulations in this framework were carried out with the PIP₂-bound mGIRK2 channel, which, according to the mechanism proposed by the Cryo-EM structures, adopts the docked conformation. Under these conditions, we do not expect a conformational change of the CTD. Thus, the coupling between the SF and the G β -binding site may be considered valid for the PIP₂-bound channel, independent of conformational changes upon PIP₂ removal.

In addition to addressing structural–biological questions, our work strives to investigate the SF mutation from a pharmacological perspective. The human GIRK2_{G154S} channel carries a mutation corresponding to the *weaver* mutation G156S in mGIRK2 and causes the rare and severe neurological Keppen–Lubinsky syndrome (KPLBS)¹³. We here present the functional and structural characterization of the human GIRK2_{G154S} disease mutant, which we show to exhibit properties strongly reminiscent of mGIRK2_{wv}, including loss of inward rectification, acquisition of sensitivity to block by the sodium channel blocker QX314, high constitutive activity and reduced K⁺ selectivity^{14,16,19}. In agreement with our electrophysiology measurements, mutant channels are permeable to both K⁺ and Na⁺ in our simulations. Na⁺ ions permeate in a partly hydrated way, while K⁺ sheds its water shell upon entry into the SF. Considering the substantial energy barrier associated with Na⁺ dehydration, the exclusion of water is likely to prevent the passing of Na⁺ flux through mGIRK2_{wv}. A similar mechanism has been reported for NaK channels⁵⁰, which narrow and dilate the SF in order to enable the permeation of dehydrated K⁺ and partially hydrated Na⁺ ions, respectively.

The replacement of G156 with a serine in mGIRK2_{wv} causes a destabilization of the SF and enables the S156 side chain to form a hydrogen bond with the backbone oxygen of I155. Hydrogen bonds surrounding the SF have been observed to form a delicate network in KcsA, which, if altered, influences the energy landscape of the filter and simultaneously the behavior of the channel⁵¹. Reminiscent of this phenomenon, the formation of the hydrogen bonds between I155 and S156 is accompanied by fundamental changes in the mGIRK2_{wv} SF. Firstly, I155 can adopt an additional conformation, which is reflected in a bimodal distribution of distances between the I155-Cas of opposing subunits. Secondly, S156 has to rotate in order to participate in the hydrogen bond, which leads to a shift in the phi backbone angle of this residue. The so-called “flipping” of SF residues, which corresponds to a rotation of the SF backbone away from the cavity and a concomitant fluctuation of the torsion angles of the affected SF residues, has previously been associated with MthK inactivation⁴⁴. The altered dynamics additionally lead to the entry of water molecules behind the SF region, which, together with the carbonyl flipping, was identified as crucial factor for SF gating of KcsA⁵¹ and MthK⁵² channels.

Na⁺ ion occupancies in mGIRK2_{wv} do not show any considerable peaks suggesting a rather accelerated flux and therefore decreased energy barriers for Na⁺ permeation. There are two main occupancy sites of K⁺ in mGIRK2_{wv}: the first one coincides with the site S3, which was also populated in mGIRK2_{wt}, while the second binding site is between S1 and S2. Importantly, both S1 and S2 are flanked by the mutated residue S156, whose deviating dynamics are likely to play a crucial role in shifting K⁺ occupancy from S2 to an in-plane position. Studies on several types of K⁺ channels directly linked ion occupancy to changes in SF conformation and gating^{44,52–55}. For example, high ion occupancies steered by the external K⁺ concentration have been associated with increased SF stability on MthK⁴⁴. Remarkably, K⁺ occupation have been reported to be crucial for MthK^{44,52} and KirBac⁵⁶ channel regulation.

We here present a mechanism underlying GIRK2 activation, which is coined by an allosteric link of the G β -binding site to the SF. This mechanism complements previously proposed hypotheses about GIRK2 regulation by suggesting the SF as an additional gate controlling K⁺ permeation. We believe that our model may be extendable to ligand-dependent modulation of other K⁺ channels, since a similar mechanism has been reported for K2P channel activation⁴⁷. Furthermore, our study is of relevance to human disease, as we present the first-time functional characterization of the human GIRK2_{G154S}. Together with our computational findings, this study will lead to a better understanding of the associated syndrome, KPLBS, and prepare the ground for therapeutic approaches targeting KPLBS and other GIRK-related diseases.

Methods

Ethical approval of *Xenopus laevis* and oocyte preparation. Oocyte experiments have been approved by Tel Aviv University Institutional Animal Care and Use Committee (permits # 01-16-104 and 01-20-083). Maintenance and surgery of female *Xenopus laevis* frogs were as described previously⁵⁷. Frogs were housed in dechlorinated water tanks, on a 10 h light/14 h dark cycle at 19 ± 2°C. Portions of ovary were removed under anesthesia with tricaine methanesulphonate (0.17%). After suturing the incision, frog was held in a separate container to fully recover from the anesthesia and then shifted to post-operational animals' tank. The frogs did not show any signs of post-operational distress and were allowed to recover for at least three months. After three to four surgeries, anaesthetized frogs were killed by decapitation and double pithing. Oocytes were defolliculated by collagenase, injected with RNA and incubated for 2–3 days at 20–22°C in ND96 solution (low K⁺) (in mM: 96 NaCl, 2 KCl, 1 MgCl₂, 1 CaCl₂, 5 HEPES, pH 7.5), supplemented with 2.5 mM sodium pyruvate and 50 µg ml⁻¹ gentamycin³⁰.

DNA constructs and RNA. DNA constructs—hGIRK2, hGIRK2_{G154S}, bovine G β ₁, and bovine G γ ₂ were cloned into high expression oocyte vectors pGEM-HE or pGEM-HJ as described previously^{58,59}. cDNA construct of hGIRK2 was kindly provided by the Tel Aviv University Blavatnik Center for Drug Discovery, in pCDNA3 vector and subcloned into pGEM-HJ vector. The predicted protein sequence corresponds to GenBank accession #NM_002240. PCR-site directed mutagenesis was performed on hGIRK2-pGEM-HJ to generate hGIRK2_{G154S}-pGEM-HJ. The mutation was confirmed by sequencing the full-length cDNA of this construct. In vitro RNA synthesis and microinjection was performed as described previously³⁰. The amounts of RNA injected per oocyte were: hGIRK2 (1 ng) or hGIRK2_{G154S} (0.5 ng), bovine G β ₁ (5 ng), and G γ ₂ (1 ng).

Electrophysiology. Whole-cell hGIRK currents were measured using the standard two-electrode voltage clamp method at 20–22°C, in high-K (HK) solution containing 8, 24, or 72 mM extracellular K⁺ concentration, [K⁺]_o²⁶. These solutions were obtained by mixing ND96 with a 96 mM K⁺ solution containing, in mM: 96 KCl, 2 NaCl, 1 CaCl₂, 1 MgCl₂, 5 HEPES, pH adjusted to 7.5 with KOH. Chemicals used in this study are listed in Supplementary Table 2. QX314 chloride was dissolved in water to a final concentration of 1 M. To study QX314 block of hGIRK2, the drug was diluted in the extracellular solutions to a final concentration of either 400 µM or 1 mM. Oocytes expressing the hGIRK2_{G154S} channels did not survive the 2-day incubation period in standard ND96 solution, presumably because of the continuous depolarization caused by Na⁺ influx via the expressed channels. Therefore, incubation of hGIRK2_{G154S}-expressing oocytes was done in the presence of 400 µM QX314, until recording. QX314 was washed out with ND96 after placing

the oocyte in the recording chamber, and the experimental protocol was started after a complete washout that took about 4–5 min. To rule out any effect from QX314 incubation, all the other groups under study, including the wild-type (WT) hGIRK2, were also subjected to QX314 incubation till the day of experiment. Oocytes expressing hGIRK2 channels and naïve oocytes were placed in a dish with ND96 solution for 4–5 min to wash off the QX314 before transferring them to recording chamber.

Current–voltage (I – V) relations were obtained using 2 s voltage ramps from –120 to +50 mV. For hGIRK2_{wt} net hGIRK I – V relationships were obtained by subtracting the current remaining after blocking all hGIRK activity with 1 mM Ba²⁺ + 26 (Fig. 3c and Supplementary Fig. 2b–d). The net I – V curves for hGIRK2_{G154S} were obtained by subtracting the averaged I – V curves obtained from naïve oocytes of the same batch from the QX-sensitive currents (Fig. 3e and Supplementary Fig. 2a, e, f).

Data analysis. I – V curves were analyzed using Clampfit 10.7 software (Molecular Devices). The reversal potential (V_{rev}) was determined from the intercept of the net I – V curve with the voltage axis. The extent of inward rectification (F_{ir}) was determined by dividing the current at 50 mV positive to V_{rev} by the current at 50 mV negative to V_{rev} (see Fig. 4e)⁶⁰:

$$F_{ir} = \frac{I_{V_{rev}+50}}{I_{V_{rev}-50}} \quad (1)$$

Estimated reversal potential (V_{rev}) was calculated using the Nernst equation:

$$V_{rev} = \frac{RT}{zF} \ln \left(\frac{[X]_{out}}{[X]_{in}} \right) \quad (2)$$

Permeability ratio, r , of sodium to potassium (pNa^+/pK^+) was determined from Goldman–Hodgkin–Katz equation:

$$E_{rev} = \frac{RT}{zF} \log \left(\frac{p_{K^+} [K^+]_o + p_{Na^+} [Na^+]_o}{p_{K^+} [K^+]_i + p_{Na^+} [Na^+]_i} \right) \quad (3)$$

For the conditions of our experiments, performed at 22 °C, we used $RT/zF = 58.17$ mV. Since the intracellular concentrations of K⁺ and Na⁺ are not exactly known, r was determined from measurement of E_{rev} (V_{rev}) in two extracellular solutions containing different K⁺ and Na⁺ concentrations, $[K_o](1)$ and $[Na_o](1)$ and $[K_o](2)$ and $[Na_o](2)$, for the pair of K⁺ external concentrations of 8 and 72 mM, as follows:

$$V_{rev} = 58.17 \log \left[\frac{[K^+]_o + r[Na^+]_o}{[K^+]_i + r[Na^+]_i} \right] \quad (4)$$

For two combinations of Na⁺ and K⁺ in external solution, 1 and 2, and with the corresponding V_{rev} measured in these solutions:

$$\frac{[K^+]_o(1) + r[Na^+]_o(1)}{[K^+]_o(2) + r[Na^+]_o(2)} = \frac{10^{\frac{V_{rev}(1)}{58.17}}}{10^{\frac{V_{rev}(2)}{58.17}}} \quad (5)$$

Denoting $\left(\frac{10^{\frac{V_{rev}(1)}{58.17}}}{10^{\frac{V_{rev}(2)}{58.17}}} \right)$ as A

$$[K^+]_o(1) + r[Na^+]_o = A[K^+]_o + rA[Na^+]_o(2); \quad (6)$$

$$r[[Na^+]_o(1) - A[Na^+]_o(2)] = A[K^+]_o(1) \quad (7)$$

$$r = \frac{A[K^+]_o(2) - [K^+]_o(1)}{[Na^+]_o(1) - [Na^+]_o(2)} \quad (8)$$

In each oocyte, the dose–response curves for Ba²⁺ inhibition of hGIRK currents were fitted to Hill equation in the form

$$\%inhibition = \frac{100\%x^h}{EC_{50}^h + x^h} \quad (9)$$

where x is the extracellular concentration of Ba²⁺, and h is Hill coefficient (slope).

Statistical analysis. Statistical analysis was performed using SigmaPlot 13 (Systat Software, Inc.) and GraphPad Prism version 8 for Windows (GraphPad Software, La Jolla, CA, USA). If the data passed the Shapiro–Wilk normality test and the equal variance test, two-group comparisons were performed using t -test, while multiple group comparison was performed using one-way ANOVA. If the data were not distributed normally, the Mann–Whitney rank sum test, or Kruskal–Wallis test were performed, respectively.

Statistics and reproducibility. All electrophysiological measurements were taken from single oocytes. The electrophysiology data are reported as mean ± SEM if the data in all test groups passed the Shapiro–Wilk normality test and the equal variance test. In most figures the results from individual cells are also shown within bars. If the data did not pass this test they were presented as box plots showing individual data points and 25th and 75th percentiles (Fig. 4d). Statistical analysis was performed using SigmaPlot 11 or 13 (Systat Software, Inc.) and GraphPad

Prism version 9 for Windows (GraphPad Software, La Jolla, CA, USA).

“Before–after” tests of an effect of a substance measured in single cells (Fig. 3f) were analyzed using paired t -test followed by Wilcoxon test. Two-group comparisons were performed using t -test if the data passed the Shapiro–Wilk normality test and the equal variance test, otherwise we used the Mann–Whitney Rank Sum Test. Multiple group comparisons were done using one-way ANOVA (ANOVA on ranks was performed whenever the data did not distribute normally). Tukey’s or Dunnett’s tests were performed for normally distributed data and Dunn’s or Kruskal–Wallis test otherwise. Statistical differences are reported in figure legends.

Molecular dynamics simulation. Gromacs (version 5.1.2)⁶¹ was used to perform molecular dynamics simulations with WT and G154S K_{ir} 3.2 channels (PDB code: 3SYA; resolution 2.98 Å, Organism: *Mus musculus*)⁵. As starting conformation, we extracted a frame of one of our previous simulations, in which mGIRK2 is in a conductive state⁷. The channels were embedded in an equilibrated 1-palmitoyl-2-oleoyl-sn-glycero-3-phosphocholine (POPC) membrane, using g_membed . Berger lipid parameters⁶² were used for lipids and the amber99sb forcefield⁶³ for the protein. PIP₂ parameters are described in our previous work⁶⁴. The system was solvated with 65,750 SPC/E water molecules⁶⁵. A total salt concentration of ~180 mM was added to the simulation system (90 mM KCl, 90 mM NaCl). The corrected monovalent Lennard–Jones parameters⁶⁶ for ions were applied and Lennard–Jones and electrostatic interactions were cut-off at 1.0 nm. Long-range electrostatic interactions were calculated every step with the Particle-Mesh Ewald algorithm⁶⁷ and bonds constrained with the LINCS algorithm⁶⁸, allowing for an integration time step of 2 fs. Temperature was coupled to 310 K using the v -rescale thermostat⁶⁹ with a coupling constant of 0.1 ps. The pressure was kept constant semi-isotropically at 1 bar with the Parrinello–Rahman⁷⁰ barostat ($\tau = 2$ ps). In the production runs, G-loop gate movement was controlled by restraining the residues G318 and M319 with 1000 kJ mol^{−1} nm^{−2} to their initial positions. During energy minimization protein atoms were restrained with a force constant of 1000 kJ mol^{−1} nm^{−2} to their starting positions. The minimization was done by using the steepest descent algorithm, followed by 10 ns of NVT and 10 ns of NPT equilibration runs.

Six runs of mGIRK2_{wt} and mGIRK2_{wt} were calculated resulting in a total simulation time of 6 μs for the wild-type and 9 μs for the mutant system (Supplementary Table 1). The runs were carried out under different electric fields of 40, 50, and 60 mV nm^{−1} along the z -axis. Taking into account the thickness of the membrane of ~3.5 nm, the electric fields yield transmembrane potentials of 140, 175, and 210 mV, respectively.

Analysis of distances and angles was conducted using Gromacs. In order to obtain average distances, the distances between opposing residues were determined and the mean of the two values calculated. The average distance between opposing I155 Cas, the average distance between F192 Cas as well as the minimum distances between F192 were considered as functional quantities for the respective functional mode analysis (FMA) models. FMA was carried out with the FMA tool developed by Hub and de Groot³⁷. As input for the FMA, we combined all frames of the MD simulation with mGIRK2_{wt} and mGIRK2_{wt} to obtain a continuous 6 and 9 μs trajectory, respectively. We performed a principle component analysis of the protein backbone and used the first 50 principle component vectors as a basis set. In order to reduce background noise, we excluded the flexible extracellular loop region (residue 120–133) and C-terminus (residue 369–382) from our model. Different allocations to model-building and cross-validation set were probed to find the division of the data, which yields the best models. For mGIRK2_{wt}, the first 2.5 μs were the basis for model building, while the last 6.5 μs were used for cross validation. For mGIRK2_{wt} the model was trained with the first 5 μs and validated with the last 1 μs. Correlation was quantified with both Pearson’s R as well as the mutual information. Visualization of the model was based on the ensemble-weighted maximally correlated motion.

Reporting summary. Further information on research design is available in the Nature Research Reporting Summary linked to this article.

Data availability

MD simulation data and source data underlying figures that support the findings of this study have been deposited in a Zenodo repository (<https://doi.org/10.5281/ZENODO.6375552>)⁷¹. Further data supporting the findings of this paper are available from the corresponding authors upon reasonable request.

Code availability

Results of electrophysiology experiments were analyzed using the Clampfit 10.7 software (Molecular Devices). Statistical analysis was performed using SigmaPlot 13 (Systat Software, Inc.) and GraphPad Prism version 8 for Windows (GraphPad Software, La Jolla California USA). Simulation trajectories were collected using the simulation program GROMACS. Visualization and analysis were performed using VMD, Pymol, Python, Java and the FMA tool. All of these software packages are publicly available.

Received: 22 July 2021; Accepted: 22 March 2022;

Published online: 11 April 2022

References

- Dascal, N. Signalling via the G protein-activated K⁺ channels. *Cell. Signal.* **9**, 551–573 (1997).
- Kurata, H. T. Emerging complexities of lipid regulation of potassium channels. *J. Gen. Physiol.* **148**, 201–205 (2016).
- Khan, S. M. et al. The expanding roles of Gβγ subunits in G protein-coupled receptor signaling and drug action. *Pharmacol. Rev.* **65**, 545–577 (2013).
- Jeremic, D., Sanchez-Rodriguez, I., Jimenez-Diaz, L. & Navarro-Lopez, J. D. Therapeutic potential of targeting G protein-gated inwardly rectifying potassium (GIRK) channels in the central nervous system. *Pharmacol. Ther.* **223**, 107808 (2021).
- Whorton, M. R. & MacKinnon, R. Crystal structure of the mammalian GIRK2 K⁺ channel and gating regulation by G-proteins, PIP2 and sodium. *Cell* **147**, 199–208 (2011).
- Whorton, M. R. & MacKinnon, R. X-ray structure of the mammalian GIRK2-βγ G protein complex. *Nature* **498**, 190–197 (2013).
- Bernsteiner, H., Zangerl-Plessl, E. M., Chen, X. & Stary-Weinzinger, A. Conduction through a narrow inward-rectifier K⁺ channel pore. *J. Gen. Physiol.* **151**, 1231–1246 (2019).
- Lacin, E. et al. Dynamic role of the tether helix in PIP2-dependent gating of a G protein-gated potassium channel. *J. Gen. Physiol.* **149**, 799–811 (2017).
- Li, D., Jin, T., Gazgalis, D., Cui, M. & Logothetis, D. E. On the mechanism of GIRK2 channel gating by phosphatidylinositol biphosphate, sodium, and the Gβγ dimer. *J. Biol. Chem.* **294**, 18934–18948 (2019).
- Niu, Y., Tao, X., Touhara, K. K. & MacKinnon, R. Cryo-EM analysis of PIP2 regulation in mammalian GIRK channels. *Elife* **9**, 60552 (2020).
- Mathiharan, Y. K. et al. Structural basis of GIRK2 channel modulation by cholesterol and PIP2. *Cell Rep.* **36**, 109619 (2021).
- Hansen, S. B., Tao, X. & MacKinnon, R. Structural basis of PIP2 activation of the classical inward rectifier K⁺ channel Kir2.2. *Nature* **477**, 495–498 (2011).
- Masotti, A. et al. Keppen–Lubinsky syndrome is caused by mutations in the inwardly rectifying K⁺ channel encoded by KCNJ6. *Am. J. Hum. Genet.* **96**, 295–300 (2015).
- Rossi, P., De Filippi, G., Armano, S., Taglietti, V. & D’Angelo, E. The weaver mutation causes a loss of inward rectifier current regulation in premigratory granule cells of the mouse cerebellum. *J. Neurosci.* **18**, 3537–3547 (1998).
- Rakic, P. & Sidman, R. L. Organization of cerebellar cortex secondary to deficit of granule cells in weaver mutant mice. *J. Comp. Neurol.* **152**, 133–161 (1973).
- Slesinger, P. A. et al. Functional effects of the mouse weaver mutation on G protein-gated inwardly rectifying K⁺ channels. *Neuron* **16**, 321–331 (1996).
- Surmeier, D. J., Mermelstein, P. G. & Goldowitz, D. The weaver mutation of GIRK2 results in a loss of inwardly rectifying K⁺ current in cerebellar granule cells. *Proc. Natl Acad. Sci. USA* **93**, 11191–11195 (1996).
- Patil, N. et al. A potassium channel mutation in weaver mice implicates membrane excitability in granule cell differentiation. *Nat. Genet.* **11**, 126–129 (1995).
- Kofuji, P. et al. Functional analysis of the weaver mutant GIRK2 K⁺ channel and rescue of weaver granule cells. *Neuron* **16**, 941–952 (1996).
- Rakic, P. & Sidman, R. L. Sequence of developmental abnormalities leading to granule cell deficit in cerebellar cortex of weaver mutant mice. *J. Comp. Neurol.* **152**, 103–132 (1973).
- Kopec, W. et al. Direct knock-on of desolvated ions governs strict ion selectivity in K⁺ channels. *Nat. Chem.* **10**, 813–820 (2018).
- Yang, L., Edvinsson, J. & Palmer, L. G. Interactions of external K⁺ and internal blockers in a weak inward-rectifier K⁺ channel. *J. Gen. Physiol.* **140**, 529–540 (2012).
- Owen, J. M., Quinn, C. C., Leach, R., Findlay, J. B. & Boyett, M. R. Effect of extracellular cations on the inward rectifying K⁺ channels Kir2.1 and Kir3.1/Kir3.4. *Exp. Physiol.* **84**, 471–488 (1999).
- Köpfer, D. A. et al. Ion permeation in K⁺ channels occurs by direct Coulomb knock-on. *Science* **346**, 352–355 (2014).
- Reuveny, E. et al. Activation of the cloned muscarinic potassium channel by G protein beta gamma subunits. *Nature* **370**, 143–146 (1994).
- Rubinstein, M., Peleg, S., Berlin, S., Brass, D. & Dascal, N. Gai3 primes the G protein-activated K⁺ channels for activation by coexpressed Gβγ in intact *Xenopus* oocytes. *J. Physiol.* **581**, 17–32 (2007).
- Zhou, H. et al. Mutations in the pore region of ROMK enhance Ba²⁺ block. *Am. J. Physiol.* **271**, C1949–C1956 (1996).
- Murata, Y., Fujiwara, Y. & Kubo, Y. Identification of a site involved in the block by extracellular Mg²⁺ and Ba²⁺ as well as permeation of K⁺ in the Kir2.1 K⁺ channel. *J. Physiol.* **544**, 665–677 (2002).
- Alagum, N., Dvir, M. & Reuveny, E. Mechanism of Ba(2+) block of a mouse inwardly rectifying K⁺ channel: differential contribution by two discrete residues. *J. Physiol.* **534**, 381–393 (2001).
- Rubinstein, M. et al. Divergent regulation of GIRK1 and GIRK2 subunits of the neuronal G protein gated K⁺ channel by GaiGDP and Gβγ. *J. Physiol.* **587**, 3473–3491 (2009).
- Kahanovitch, U. et al. Recruitment of Gβγ controls the basal activity of G-protein coupled inwardly rectifying potassium (GIRK) channels: crucial role of distal C terminus of GIRK1. *J. Physiol.* **592**, 5373–5390 (2014).
- Noskov, S. Y. & Roux, B. Ion selectivity in potassium channels. *Biophys. Chem.* **124**, 279–291 (2006).
- Thompson, A. N. et al. Mechanism of potassium-channel selectivity revealed by Na⁺ and Li⁺ binding sites within the KcsA pore. *Nat. Struct. Mol. Biol.* **16**, 1317–1324 (2009).
- Guidoni, L., Torre, V. & Carloni, P. Potassium and sodium binding to the outer mouth of the K⁺ channel †. *Biochemistry* **38**, 8599–8604 (1999).
- Bucher, D., Guidoni, L., Carloni, P. & Rothlisberger, U. Coordination numbers of K⁺ and Na⁺ ions inside the selectivity filter of the KcsA potassium channel: insights from first principles molecular dynamics. *Biophys. J.* **98**, L47–L49 (2010).
- McCoy, J. G. & Nimigean, C. M. Structural correlates of selectivity and inactivation in potassium channels. *Biochim. Biophys. Acta-Biomebr.* **1818**, 272–285 (2012).
- Hub, J. S. & De Groot, B. L. Detection of functional modes in protein dynamics. *PLoS Comput. Biol.* **5**, e1000480 (2009).
- Chatelain, F. C. et al. The pore helix dipole has a minor role in inward rectifier channel function. *Neuron* **47**, 833–843 (2005).
- Jiang, Y. & MacKinnon, R. The barium site in a potassium channel by x-ray crystallography. *J. Gen. Physiol.* **115**, 269–272 (2000).
- Wang, W., Touhara, K. K., Weir, K., Bean, B. P. & MacKinnon, R. Cooperative regulation by G proteins and Na⁺ of neuronal GIRK2 K⁺ channels. *Elife* **5**, 1–15 (2016).
- Wang, W., Whorton, M. R. & MacKinnon, R. Quantitative analysis of mammalian GIRK2 channel regulation by G proteins, the signaling lipid PIP2 and Na⁺ in a reconstituted system. *Elife* **3**, e03671 (2014).
- Li, D. L., Hu, L., Wang, L. & Chen, C. L. Permeation mechanisms through the selectivity filter and the open helix bundle crossing gate of GIRK2. *Comput. Struct. Biotechnol. J.* **18**, 3950–3958 (2020).
- Jarolimex, W., Bäurle, J. & Misgeld, U. Pore mutation in a G-protein-gated inwardly rectifying K⁺ channel subunit causes loss of K⁺-dependent inhibition in weaver hippocampus. *J. Neurosci.* **18**, 4001–4007 (1998).
- Kopec, W., Rothberg, B. S. & de Groot, B. L. Molecular mechanism of a potassium channel gating through activation gate-selectivity filter coupling. *Nat. Commun.* **10**, 1–15 (2019).
- Labro, A. J., Marien Cortes, D., Tilegenova, C. & Cuello, L. G. Inverted allosteric coupling between activation and inactivation gates in K⁺ channels. *Proc. Natl Acad. Sci. USA* **115**, 5426–5431 (2018).
- Brettmann, J. B., Urusova, D., Tonelli, M., Silva, J. R. & Henzler-Wildman, K. A. Role of protein dynamics in ion selectivity and allosteric coupling in the NaK channel. *Proc. Natl Acad. Sci. USA* **112**, 15366–15371 (2015).
- Zhuo, R. G. et al. Allosteric coupling between proximal C-terminus and selectivity filter is facilitated by the movement of transmembrane segment 4 in TREK-2 channel. *Sci. Rep.* **6**, 1–9 (2016).
- Chen, I., Eldstrom, J., Fedida, D. & Kubo, Y. A novel ion conducting route besides the central pore in an inherited mutant of G-protein-gated inwardly rectifying K⁺ channel. *J. Physiol.* **0**, 1–20 (2021).
- Jin, T. et al. The βγ subunits of G proteins gate a K⁺ channel by pivoted bending of a transmembrane segment. *Mol. Cell* **10**, 469–481 (2002).
- Shi, C. et al. A single NaK channel conformation is not enough for non-selective ion conduction. *Nat. Commun.* **9**, 1–8 (2018).
- Jekhmene, S. et al. Shifts in the selectivity filter dynamics cause modal gating in K⁺ channels. *Nat. Commun.* **10**, 1–12 (2019).
- Boiteux, C., Posson, D. J., Allen, T. W. & Nimigean, C. M. Selectivity filter ion binding affinity determines inactivation in a potassium channel. *Proc. Natl Acad. Sci. USA* **117**, 29968–29978 (2020).
- Zhou, Y. & MacKinnon, R. The occupancy of ions in the K⁺ selectivity filter: charge balance and coupling of ion binding to a protein conformational change underlie high conduction rates. *J. Mol. Biol.* **333**, 965–975 (2003).
- Edvinsson, J. M., Shah, A. J. & Palmer, L. G. Kir4.1 K⁺ channels are regulated by external cations. *Channels* **5**, 269–279 (2011).
- Lolicato, M. et al. K2P channel C-type gating involves asymmetric selectivity filter order-disorder transitions. *bioRxiv* 1–13 <https://doi.org/10.1101/2020.03.20.000893> (2020).
- Clarke, O. B. et al. Domain reorientation and rotation of an intracellular assembly regulate conduction in kir potassium channels. *Cell* **141**, 1018–1029 (2010).
- Dascal, N. & Lotan, I. Expression of exogenous ion channels and neurotransmitter receptors in RNA-injected *Xenopus* oocytes. In *Protocols in Molecular Neurobiology* (eds Longstaff, A. & Revest, P.) 205–225 (Springer, New York, 1992).
- Berlin, S. et al. Two distinct aspects of coupling between Gai protein and G protein-activated K⁺ channel (GIRK) revealed by fluorescently labeled Gai3 protein subunits. *J. Biol. Chem.* **286**, 33223–33235 (2011).

59. Rishal, I., Porozov, Y., Yakubovich, D., Varon, D. & Dascal, N. G β y-dependent and G β y-independent basal activity of G protein-activated K⁺ channels. *J. Biol. Chem.* **280**, 16685–16694 (2005).
60. Hommers, L. G., Lohse, M. J. & Bünemann, M. Regulation of the inward rectifying properties of G-protein-activated inwardly rectifying K⁺ (GIRK) channels by Gbeta gamma subunits. *J. Biol. Chem.* **278**, 1037–1043 (2003).
61. Abraham, M. J. et al. Gromacs: high performance molecular simulations through multi-level parallelism from laptops to supercomputers. *SoftwareX* <https://doi.org/10.1016/j.softx.2015.06.001> (2015).
62. Berger, O., Edholm, O. & Jähnig, F. Molecular dynamics simulations of a fluid bilayer of dipalmitoylphosphatidylcholine at full hydration, constant pressure, and constant temperature. *Biophys. J.* **72**, 2002–2013 (1997).
63. Hornak, V. et al. Comparison of multiple amber force fields and development of improved protein backbone parameters vikor. *Proteins Struct. Funct. Bioinforma.* **65**, 712–725 (2006).
64. Lee, S.-J. et al. Structural basis of control of inward rectifier Kir2 channel gating by bulk anionic phospholipids. *J. Gen. Physiol.* **148**, 227–237 (2016).
65. Berendsen, H. J. C., Grigera, J. R. & Straatsma, T. P. The missing term in effective pair potentials. *J. Phys. Chem.* **91**, 6269–6271 (1987).
66. Jung, I. S. & Cheatham, T. E. Determination of alkali and halide monovalent ion parameters for use in explicitly solvated biomolecular simulations. *J. Phys. Chem. B* **112**, 9020–9041 (2008).
67. Essmann, U. et al. A smooth particle mesh Ewald method. *J. Chem. Phys.* **103**, 8577–8593 (1995).
68. Hess, B., Bekker, H., Berendsen, H. J. C. & Fraaije, J. G. E. M. LINCS: a linear constraint solver for molecular simulations. *J. Comput. Chem.* **18**, 1463–1472 (1997).
69. Bussi, G., Donadio, D. & Parrinello, M. Canonical sampling through velocity rescaling. *J. Chem. Phys.* **126**, 7 (2007).
70. Parrinello, M. & Rahman, A. Polymorphic transitions in single crystals: a new molecular dynamics method. *J. Appl. Phys.* **52**, 7182–7190 (1981).
71. Friesacher, T. et al. A selectivity filter mutation provides insights into gating regulation of a K⁺ channel <https://doi.org/10.5281/ZENODO.6375552> (2022).

Acknowledgements

The computational results presented have been achieved in part using the Vienna Scientific Cluster (VSC). This work was supported by the doctoral program “Molecular drug targets” W1232 (T.F. and A.S.-W.) and the Post-Doc program “Zukunftskolleg” ZK-81B of the Austrian Science Fund (FWF) (T.F. and E.-M. Z.-P.), the DOC fellowship 26156 of the Austrian Academy of Sciences (ÖAW) (T.F.), the Israel-India Binational grant (Israeli # ISF_2255_2015 and Indian # UGC-6-1/2016 (1C) (N.D. and A.K.B); Israel Science Foundation grant # ISF_1282_2018 (N.D.).

Author contributions

A.S.-W., T.F., and H.B. conceived the computational design of the project. T.F. and H.B. carried out molecular modeling, which was analyzed by A.S.-W., T.F., H.B., and E.-M.Z.-P. Experiments were designed by N.D. and H.P.R. and carried out by H.P.R., B.S., and J.C.C. A.S.-W., T.F., N.D., and H.P.R. wrote the paper, with contributions from H.B., A.K.B., and E.-M.Z.-P.

Competing interests

The authors declare no competing interests.

Additional information

Supplementary information The online version contains supplementary material available at <https://doi.org/10.1038/s42003-022-03303-1>.

Correspondence and requests for materials should be addressed to Nathan Dascal or Anna Sary-Weinzinger.

Peer review information *Communications Biology* thanks Diomedes Logothetis and the other, anonymous, reviewer(s) for their contribution to the peer review of this work. Primary handling editors: Eliana Scemes, Anam Akhtar, and George Inglis. Peer reviewer reports are available.

Reprints and permission information is available at <http://www.nature.com/reprints>

Publisher's note Springer Nature remains neutral with regard to jurisdictional claims in published maps and institutional affiliations.



Open Access This article is licensed under a Creative Commons Attribution 4.0 International License, which permits use, sharing, adaptation, distribution and reproduction in any medium or format, as long as you give appropriate credit to the original author(s) and the source, provide a link to the Creative Commons license, and indicate if changes were made. The images or other third party material in this article are included in the article's Creative Commons license, unless indicated otherwise in a credit line to the material. If material is not included in the article's Creative Commons license and your intended use is not permitted by statutory regulation or exceeds the permitted use, you will need to obtain permission directly from the copyright holder. To view a copy of this license, visit <http://creativecommons.org/licenses/by/4.0/>.

© The Author(s) 2022